

THE SPATIAL COMPLEXITY OF LOCALIZED BUCKLING IN RODS WITH NONCIRCULAR CROSS SECTION*

G. H. M. VAN DER HEIJDEN[†], A. R. CHAMPNEYS[‡], AND J. M. T. THOMPSON[†]

Abstract. We study the postbuckling behavior of long, thin elastic rods subject to end moment and tension. This problem in statics has the well-known Kirchhoff dynamic analogy in rigid body mechanics consisting of a reversible three-degrees-of-freedom Hamiltonian system. For rods with noncircular cross section, this dynamical system is in general nonintegrable and in dimensionless form depends on two parameters: a unified load parameter and a geometric parameter measuring the anisotropy of the cross section.

Previous work has given strong evidence of the existence of a countable infinity of localized buckling modes which in the dynamic analogy correspond to N -pulse homoclinic orbits to the trivial solution representing the straight rod. This paper presents a systematic numerical study of a large sample of these buckling modes. The solutions are found by applying a recently developed shooting method which exploits the reversibility of the system. Subsequent continuation of the homoclinic orbits as parameters are varied then yields load-deflection diagrams for rods with varying load and anisotropy. From these results some structure in the multitude of buckling modes can be found, allowing us to present a coherent picture of localized buckling in twisted rods.

Key words. anisotropic rods, torsional buckling, spatial chaos, homoclinic orbits, bifurcation

AMS subject classifications. 73K05, 34C37, 58F14

PII. S0036139996306833

1. Introduction. This paper extends the work of [9, 24] on the classic problem of the postbuckling behavior of long, thin, initially straight elastic rods subject to end moment and tension. The reader is referred to [1, 9, 24] and references therein for the long history of this problem, together with its importance in a range of practical situations such as DNA formation, failure of undersea cables, and oil-well drill string buckling.

For rods with circular cross section, it was shown in [24], both experimentally and via energy analysis, that a localized form is the preferred mode of buckling for sufficiently long rods under a variety of different loading configurations. These results were matched in [9] by theoretical and numerical analysis of the celebrated Kirchhoff–Love equations which govern the spatial equilibria of thin elastic rods and may be regarded as a special case of the general Cosserat formulation of rod mechanics (see [1, Chap. VIII]). In the limit of infinitely long rods, one may use the analogy with an initial-value problem. The Kirchhoff–Love equations then constitute a reversible, sixth-order Hamiltonian dynamical system subject to two additional integral constraints, and localized buckling modes correspond to homoclinic orbits to the trivial solution representing a straight rod. In particular, in [9] it was shown that the buckling process can be explained by the bifurcation of a homoclinic solution as a single dimensionless load parameter is varied.

Extra complications arise when the cross section of the rod is not circular, or more specifically when the bending stiffnesses about two orthogonal planes are not

*Received by the editors July 17, 1996; accepted for publication (in revised form) April 11, 1997; published electronically October 26, 1998.

<http://www.siam.org/journals/siap/59-1/30683.html>

[†]Centre for Nonlinear Dynamics, University College London, Gower Street, London WC1E 6BT, UK (g.heijden@ucl.ac.uk, jmtt@ucl.ac.uk).

[‡]Department of Engineering Mathematics, University of Bristol, University Walk, Bristol BS8 1TR, UK (a.r.champneys@bristol.ac.uk).

equal. The Kirchhoff–Love equations then cease in general to be completely integrable [23], and strong evidence indicates that there exist a countable infinity of potential localized buckling modes, explained as follows. In agreement with normal-form analysis near a Hamiltonian–Hopf bifurcation in a reversible system [20], the twisted rod was numerically found to possess four primary buckling modes. Then, in agreement with the theory of Devaney [12] and the transversality result proved in [23], numerical evidence was found of the existence of an infinity of multimodal localized buckling responses. In the dynamic analogy such solutions correspond to N -pulse homoclinic orbits and approximately consist of N translations of a primary homoclinic solution. It was noted in [9] that the situation sketched above has strong parallels to the simpler case of a strut resting on a nonlinear elastic foundation [16, 17, 8, 4].

The contribution of the present paper is to present a comprehensive numerical investigation of a large family of localized buckling modes indicated to occur in [9]. Specifically, we apply a shooting method developed in [7] to compute a systematic sample of the primary and multimodal homoclinic orbits. Subsequent use of the continuation code AUTO [13, 14] then allows us to study these solutions when parameters in the system are varied and to find some structure in the multitude of buckling modes. Our particular aim is to plot bifurcation diagrams showing how either axial rotation or end shortening varies against a unified load parameter (representing either applied moment or tension). From such diagrams one may draw predictions as to what should occur under a variety of physical loading conditions, either rigid (end shortening and/or rotation controlled) or dead (tension and/or end moment controlled). We also consider the effects of variations in a parameter measuring the degree of anisotropy of the rod’s cross section in order to contrast, for example, the buckling characteristics of nearly circular rods with those of thin tapes.

The rest of the paper is outlined as follows. Section 2 recalls the Kirchhoff–Love formulation and its nondimensionalization that is used throughout the rest of the paper. Section 3 concerns shooting methods applied to the computation of homoclinic orbits at fixed load levels, which are shown to be in keeping with theoretical multiplicity results. Section 4 then presents bifurcation diagrams obtained for these solutions upon varying the load or anisotropy parameters. Finally, in section 5, we draw conclusions about the physical implications of our results and suggest future directions of research.

2. The mathematical model. Consider the classic problem of determining the equilibrium configuration of a long, thin elastic rod which when subject to no external forces is straight and prismatic with uniform cross section. Suppose, as an idealization for long rods, that the rod is infinitely long. For the present investigations we shall make further idealizations by ignoring the effects of shear deformation and axial extension and assuming that the constitutive laws are linear in appropriate coordinates. For a more complete derivation including these and other effects, the reader is referred to [1, 9, 22].

The formulation of equilibrium equations begins by choosing a rod-centered coordinate system with axes $\mathbf{e}_1(s), \mathbf{e}_2(s), \mathbf{e}_3(s)$ that are fixed to the material of the rod and that vary along its axial arc length s . \mathbf{e}_3 is chosen to be everywhere tangent to the axis of the rod, and the three axes align with fixed Cartesian (x, y, z) axes when the rod is unstrained. The strain of the rod is measured by the vector

$$\Omega(s) = \kappa_1(s) \mathbf{e}_1(s) + \kappa_2(s) \mathbf{e}_2(s) + \tau(s) \mathbf{e}_3(s),$$

where τ is the twist about the body axis of the rod and $\kappa_{1,2}$ are the principal curva-

tures. Let

$$\mathbf{F}(s) = F_1(s) \mathbf{e}_1(s) + F_2(s) \mathbf{e}_2(s) + F_3(s) \mathbf{e}_3(s)$$

and

$$\mathbf{G}(s) = G_1(s) \mathbf{e}_1(s) + G_2(s) \mathbf{e}_2(s) + G_3(s) \mathbf{e}_3(s)$$
 be the respective resultant force

and couple exerted by the material in the direction of increasing s . Here, $F_{1,2}$ are shear forces, F_3 is tension, $G_{1,2}$ are bending moments about the axes $\mathbf{e}_{1,2}$, and G_3 is the twisting moment about the centerline. We assume linear constitutive relations of the form

$$(2.1) \quad \kappa_1 = G_1/A, \quad \kappa_2 = G_2/B, \quad \tau = G_3/C,$$

where A and B are the principal bending stiffnesses (about the \mathbf{e}_1 and \mathbf{e}_2 axes, respectively) and C is the torsional stiffness of the rod.

Using (2.1) it is possible to write down, via force and moment balance, equilibrium equations with the components of \mathbf{F} and \mathbf{G} as the dependent variables. As boundary conditions we assume that a moment M and tension T are applied in the direction \mathbf{e}_3 at $s = \pm\infty$. In the dimensionless variables

$$(2.2) \quad \begin{aligned} t &= (M/B)s, \quad x_1 = F_1/T, \quad x_2 = F_2/T, \quad x_3 = (F_3 - T)/T \\ x_4 &= G_1/M, \quad x_5 = G_2/M, \quad x_6 = (G_3 - M)/M, \end{aligned}$$

the equilibrium equations become [9]

$$(2.3) \quad \begin{aligned} \dot{x}_1 &= (1 + \nu)x_2(1 + x_6) - (1 + x_3)x_5, \\ \dot{x}_2 &= (1 + \rho)(1 + x_3)x_4 - (1 + \nu)x_1(1 + x_6), \\ \dot{x}_3 &= x_1x_5 - (1 + \rho)x_2x_4, \\ \dot{x}_4 &= \nu x_5(1 + x_6) + x_2/m^2, \\ \dot{x}_5 &= (\rho - \nu)x_4(1 + x_6) - x_1/m^2, \\ \dot{x}_6 &= -\rho x_4x_5 \end{aligned}$$

subject to the boundary conditions

$$(2.4) \quad (x_1, x_2, x_3, x_4, x_5, x_6) \rightarrow (0, 0, 0, 0, 0, 0) \quad \text{as } t \rightarrow \pm\infty.$$

Here, the overdot “.” denotes differentiation with respect to the scaled arc length t , and

$$(2.5) \quad m = M/\sqrt{BT}, \quad \rho = (B/A) - 1, \quad \nu = (B/C) - 1$$

are dimensionless parameters. m is a single unified load parameter, showing the equivalence between increasing moment and reducing tension. ρ is an anisotropy parameter which is zero for rods whose principal bending stiffnesses are equal, as would be the case for either a circular or square cross section. Without loss of generality we can take $B > A$ and assume ρ to be nonnegative. Finally, ν measures the ratio of bending to torsional stiffness: For circular rods ν is equal to Poisson’s ratio. We shall keep $\nu = \frac{1}{3}$ throughout the rest of this paper, as this is a typical value of Poisson’s ratio for, e.g., steel (see [24]). It should be stressed, however, that for ρ nonzero, ν no longer equals Poisson’s ratio. See [25] for the relationship between (ρ, ν) and (aspect ratio, Poisson’s ratio) for rods with, for example, elliptical cross section.

To interpret solutions of (2.3) in terms of the fixed coordinate system (x, y, z) we have to solve (2.3) along with the Frenet–Serret equations of differential geometry (cf. [22, Art. 253]),

$$(2.6) \quad \dot{\mathbf{e}}_i = \tilde{\Omega} \times \mathbf{e}_i, \quad i = 1, 2, 3,$$

as well as the defining equations for the rod's centerline,

$$(2.7) \quad \dot{\mathbf{r}} = \mathbf{e}_3.$$

$\tilde{\Omega} := (1 + \rho)x_4 \mathbf{e}_1 + x_5 \mathbf{e}_2 + (1 + \nu)(1 + x_6) \mathbf{e}_3$ is the dimensionless strain vector and $\mathbf{r} = (r_1, r_2, r_3)$ denotes the dimensionless vector position of the centerline in the fixed coordinates.

If one solves an initial-value problem, that is, if, in place of (2.4), one specifies the initial conditions for \mathbf{x} exactly, then notice that (2.6) and (2.7) are slaved to (2.3). They merely postprocess the solutions of (2.3) to give the actual configuration of the rod. Treated in this way, (2.3) is a conservative dynamical system (Kirchhoff's dynamic analogy) with Hamiltonian function

$$(2.8) \quad H = 2x_3 + m^2[(1 + \rho)x_4^2 + x_5^2 + (1 + \nu)(x_6 + 1)^2],$$

which is related to the strain energy function of elasticity theory. It is known (see, e.g., [23]) that (2.3) has two integrals of the motion corresponding to conservation along the axial length of the rod of the magnitude of force and the component of torque about the loading axis. In the present notation,

$$(2.9) \quad I_1 := x_1^2 + x_2^2 + (x_3 + 1)^2 = \text{const.},$$

$$(2.10) \quad I_2 := x_1x_4 + x_2x_5 + (1 + x_3)(1 + x_6) = \text{const.}$$

We should remark that (2.8), (2.9), and (2.10) do not represent three independent isolating integrals of (2.3) and therefore the Hamiltonian system is not necessarily completely integrable. In fact, it is possible to use (2.9) and (2.10) to reduce (2.3) further to a four-dimensional system, see, e.g., [23, 25]. In any case, solutions of (2.3) with given I_1 and I_2 are restricted to a four-dimensional phase space within \mathbb{R}^6 . Moreover, in the case of a circular rod, i.e., when $\rho = 0$, we have the obvious additional integral

$$(2.11) \quad I_3 := x_6 = \text{const.},$$

which is independent of (2.9) and (2.10), and hence the system is completely integrable, implying that motion occurs on 3-tori. Physically, this integral corresponds to the conserved torque about the body axis \mathbf{e}_3 of the rod.

Note that the system (2.3) is invariant under the action of \mathbb{Z}_2 given by

$$(2.12) \quad Z : (x_1, x_2, x_3, x_4, x_5, x_6) \rightarrow (-x_1, -x_2, x_3, -x_4, -x_5, x_6).$$

Thus all nontrivial solutions come in pairs of Z images of each other. Physically, this corresponds to a rotation of 180° about the z axis (the centerline of the unstrained rod), which is related to the rod's invariance under a 180° rotation about its centerline. Another property of importance is the invariance of (2.3) under the reversing involutions

$$(2.13) \quad R_1 : (x_1, x_2, x_3, x_4, x_5, x_6) \rightarrow (-x_1, x_2, x_3, -x_4, x_5, x_6), \quad t \rightarrow -t,$$

$$(2.14) \quad R_2 : (x_1, x_2, x_3, x_4, x_5, x_6) \rightarrow (x_1, -x_2, x_3, x_4, -x_5, x_6), \quad t \rightarrow -t,$$

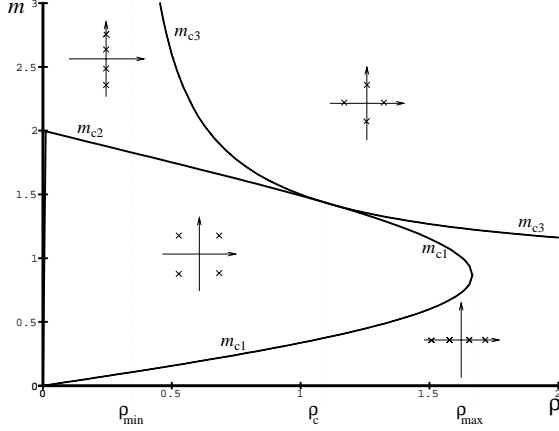


FIG. 2.1. Loci of bifurcation points and eigenvalue configurations in the ρ - m parameter plane for $\nu = \frac{1}{3}$. $\rho_{\min} = 0.3333$, $\rho_c = 1.1064$, $\rho_{\max} = 1.6667$. The buckling line is formed by the union of m_{c2} and the part of m_{c3} to the right of ρ_c .

which satisfy $R_1 R_2 = Z$.

Linearization of (2.3) about $\mathbf{x} = \mathbf{0}$ yields the characteristic polynomial

$$(2.15) \quad \lambda^6 + [2\nu^2 + (2 - \rho)\nu + 1 - (\rho + 2)/m^2]\lambda^4 + [\nu^4 + (2 - \rho)\nu^3 + (1 - 2\rho)\nu^2 - \nu\rho + ((2 + \rho)\nu^2 + 2\nu - \rho)/m^2 + (1 + \rho)/m^4]\lambda^2.$$

Note that there are always two zero eigenvalues whose eigenvectors, aligned along the x_3 and x_6 axes, correspond to the directions ∇I_1 and ∇I_2 given by the integrals (2.9) and (2.10). The remaining four eigenvalues have eigenspaces which are orthogonal to these axes. By setting (2.15) and its λ derivative equal to zero we can find a condition for double eigenvalues:

$$(2.16) \quad \rho^2 m^{-4} + (-16\nu - 16\nu^2 - 8\rho\nu^2 + 2\rho - 4 + 2\rho^2\nu)m^{-3} + 4\rho\nu^2 + 4\nu^2 + 1 + 4\nu + 2\rho\nu + \rho^2\nu^2 = 0.$$

Solutions of (2.16) are presented in Fig. 2.1 as the curves m_{c1} and m_{c2} . The curve m_{c1} corresponds to a real-to-complex eigenvalue transition, and m_{c2} to a Hamiltonian–Hopf line, where a complex quadruple of eigenvalues become imaginary as m increases. Also shown in this figure is the curve m_{c3} of points where two eigenvalues pass through zero (i.e., where the coefficient of λ^2 in (2.15) vanishes). In [9, 24], it was noted that m_{c2} , for small ρ , corresponds to the classic critical buckling load of the rod. The trivial equilibrium configuration is physically stable (under dead loading) for $m < m_{c2}$ and unstable for $m > m_{c2}$. Note the distinction between stability of physical configurations (an infinite-dimensional problem) and the stability of states of the finite-dimensional dynamical system (2.3).

Normal-form analysis by Iooss and Pérouème [20] shows that at a Hamiltonian–Hopf bifurcation in a reversible system, given a condition on the sign of a certain coefficient, generically a pair of symmetric homoclinic orbits bifurcate subcritically (i.e., for $m < m_{c_2}$). Given the two involutions R_1 and R_2 above, their analysis would then show that at least four homoclinic orbits bifurcate, two for each of R_1 and R_2 . In [25] the normal-form coefficient for this system is calculated and found to be of the appropriate sign.

The critical values ρ_c and ρ_{\max} in Fig. 2.1 are found to be given by (see [9])

$$(2.17) \quad \rho_c = \frac{3\nu^2 - 1 + \sqrt{9\nu + 5}(\nu + 1)^{\frac{3}{2}}}{4\nu + 2},$$

$$(2.18) \quad \rho_{\max} = 2\nu + 1,$$

while the asymptote of m_{c_3} is

$$(2.19) \quad \rho_{\min} = \nu.$$

The codimension-2 point at ρ_c will play an important role in distinguishing between two types of buckling behavior (for $\rho < \rho_c$ and $\rho > \rho_c$); see section 4 below and [25].

3. Numerical results for fixed parameter values.

3.1. The shooting method. In this section we numerically compute approximations to localized buckling responses by looking for solutions of (2.3) that satisfy approximations of the homoclinic boundary conditions (2.4). Specifically, we truncate the “time” interval to $[0, \mathcal{T}]$ and, following Beyn [3], apply the left-hand boundary conditions

$$(3.1) \quad x_3(0) = x_6(0) = 0,$$

$$(3.2) \quad L_s(m)\mathbf{x}(0) = \mathbf{0},$$

where $L_s(m)$ is the projection matrix onto the *left* eigenspace corresponding to the stable eigenvalues $-\lambda \pm i\omega$ (recall from Fig. 2.1 that for $\rho < \rho_c$ and $m_{c_1} < m < m_{c_2}$ the trivial equilibrium has eigenvalues of the form $0, 0, \pm\lambda \pm i\omega$). Note that (3.1) in effect fixes the values of the integrals I_1 and I_2 , while (3.2) places solutions in the linearized unstable manifold of the origin.

Because our system is reversible, an appropriate right-hand boundary condition is to place the solution in the symmetric section of either of the reversing transformations R_1 or R_2 , i.e.,

$$(3.3) \quad x_1(\mathcal{T}) = x_4(\mathcal{T}) = 0,$$

or

$$(3.4) \quad x_2(\mathcal{T}) = x_5(\mathcal{T}) = 0,$$

respectively. Equation (2.3) subject to (3.1), (3.2), and (3.3) or (3.4) is a suitable boundary-value problem for one-parameter continuation of homoclinic solutions, provided \mathcal{T} is sufficiently large. There is a well-developed error theory for such boundary-value problems (see [3, 6] and references therein) showing that the convergence of approximate solutions to a true homoclinic solution is exponential in \mathcal{T} . In what follows we solve such boundary-value problems using AUTO [13, 14].

TABLE 3.1
Primary homoclinic orbits ($\nu = \frac{1}{3}$, $\rho = 0.5$, $m = 1.7$).

Label	δ	Midpoint \mathcal{T}	Reversible under
P_1	6.066428	71.498592	R_1
P_2	2.924836	71.498592	R_1
P_3	1.331789	71.467436	R_2
P_4	4.473381	71.467436	R_2

In order to produce a solution at a fixed parameter value, it is easier and more instructive to use a shooting approach based on solving an initial-value problem (cf. [7]). For this purpose we replace (3.1), (3.2) by the initial conditions

$$(3.5) \quad \mathbf{x}(0) = \varepsilon(\mathbf{v}_1 \cos \delta + \mathbf{v}_2 \sin \delta),$$

where $\mathbf{v}_1 \pm i\mathbf{v}_2$ are eigenvectors corresponding to $\lambda \pm i\omega$, ε is small, and $0 \leq \delta < 2\pi$. Fixing ε , in effect, determines the length of the interval \mathcal{T} over which we have to solve. In the computations that follow we have guarded against spurious numerical solutions by repeating some runs using a variety of values of ε . In practice we found that $\varepsilon = 10^{-5}$ was sufficiently small to produce reliable solutions. Solutions of the initial-value problems in the shooting method were solved using a highly accurate numerical integration routine (*d02cbf* from the NAG library) with local error tolerance 10^{-14} . Solutions over the *finite* time intervals in question were found to conserve the integrals I_1, I_2 to approximately within this tolerance.

In order to compute load-deflection bifurcation diagrams for localizing solutions it is necessary to also measure the end displacement D and end rotation R from the straight-rod position. Therefore, we solve the 18 equations (2.3), (2.6), (2.7) subject to the initial conditions (3.5) and

$$(3.6) \quad \mathbf{r}(0) = (0, 0, 0), \quad \mathbf{e}_1(0) = (1, 0, 0), \quad \mathbf{e}_2(0) = (0, 1, 0), \quad \mathbf{e}_3(0) = (0, 0, 1).$$

The end displacement and end rotation can then be obtained as

$$(3.7) \quad D = \mathcal{T} - r_3(\mathcal{T}), \quad \cos R = \langle \mathbf{e}_1(\mathcal{T}), (1, 0, 0) \rangle, \quad \sin R = \langle \mathbf{e}_1(\mathcal{T}), (0, 1, 0) \rangle,$$

provided $\mathbf{e}_3(\mathcal{T})$ is sufficiently aligned with the initial direction $\mathbf{e}_3(0) = (0, 0, 1)$. Although the angle R is only defined modulo 2π in (3.7), continuity with respect to the arc length parameter t will allow us to keep track of the number of full turns made by the end point. Equations (2.3) with initial conditions (3.5) coupled to (2.6) and (2.7) with initial conditions (3.6) form a well-defined problem for the shooting approach developed in [7] for homoclinic orbits in reversible systems. Varying the two parameters δ and \mathcal{T} , we can satisfy either of the boundary conditions (3.3) or (3.4).

Remark. By using the symmetric section in the numerical scheme sketched above, we only have to integrate half the orbit. The price we pay is that in this way only solutions invariant under R_1 or R_2 will be found. To find other solutions and see how they interact with R_1 - or R_2 -symmetric ones we have to shoot over the whole length of the rod, replacing the right-hand boundary conditions (3.3) or (3.4) by the equivalent of the projection boundary condition (3.2) but now projecting out the unstable directions (see, for example, [21]).

TABLE 3.2

Selected data for three sequences of bimodal and two sequences of 4-modal homoclinic orbits ($\nu = \frac{1}{3}$, $\rho = 0.5$, $m = 1.7$).

n	δ_n	\mathcal{T}_n	$\mathcal{T}_n - \mathcal{T}_{n-1}$
1	6.238174	99.141596	
2	5.979388	101.085293	1.943697
3	6.104248	103.593991	2.508697
4	6.048636	105.837107	2.243117
5	6.074524	108.200094	2.362987
6	6.062687	110.507630	2.307535
7	6.068146	112.840573	2.332943
8	6.065638	115.161820	2.321247
9	6.066792	117.488441	2.326620
10	6.066261	119.812591	2.324150
11	6.066505	122.137876	2.325285
12	6.066393	124.462639	2.324763
13	6.066445	126.787643	2.325003
14	6.066421	129.112536	2.324893
15	6.066432	131.437480	2.324944
P_1	6.066428	71.498592	$\frac{\pi}{2\omega} = 2.324928$

3.2. A multitude of homoclinic orbits. As stated earlier, all numerical experiments will be carried out using the typical value $\nu = \frac{1}{3}$. Initially, in order to compute a sample of homoclinic orbits for fixed parameter values, we further fix $\rho = 0.5$, $m = 1.7$. The eigenvalues corresponding to the unstable manifold of the origin then are $\lambda \pm i\omega$, where $\lambda = 0.167015$, $\omega = 0.675632$. In (3.5) we use

$$\begin{aligned} \mathbf{v}_1 &= (0.696351, 0.0562830, 0, 0.381032, -0.0412567, 0), \\ \mathbf{v}_2 &= (0, 0.542187, 0, 0.0857199, 0.252439, 0), \end{aligned}$$

and $\varepsilon = 10^{-5}$. Using our shooting algorithm in which we vary δ in (3.5) in order to satisfy one of the right-hand boundary conditions (3.3) or (3.4), we find the four primary homoclinic orbits given in Table 3.1. Plots of these solutions in physical space are shown in Fig. 3.1. Note that for each involution we have a pair of orbits with δ values differing by π , reflecting the \mathbb{Z}_2 symmetry of the system. Hence, the multiplicity of primary homoclinic orbits found is consistent with the normal-form theory mentioned in section 2.

Recall that the system (2.3) may be regarded as a reversible Hamiltonian system evolving in a four-dimensional phase space. For such Hamiltonian systems with complex eigenvalues, the theory of Devaney [12] can be used to show that the existence of one homoclinic orbit generically implies the existence of an infinity of others. See also [2, 4] and, for reversible systems, [5, 15]. The extra solutions are multimodal, like multiple copies of the primary, and can be labeled by finite strings of integers indicating the number of turns the homoclinic orbit makes around the equilibrium between copies. The key nondegeneracy condition is the transversality around the primary homoclinic solution of the intersection of the stable and unstable manifolds. Such a result is known for the simpler four-dimensional model of a strut resting on a nonlinear elastic foundation [16, 17, 8, 4], which has many similarities with the problem under investigation here (see [9] for a comparison). For the present problem, Mielke and Holmes [23] have shown the required transversality condition using Melnikov analysis for small perturbations of the integrable limit (small ρ in our notation). Away

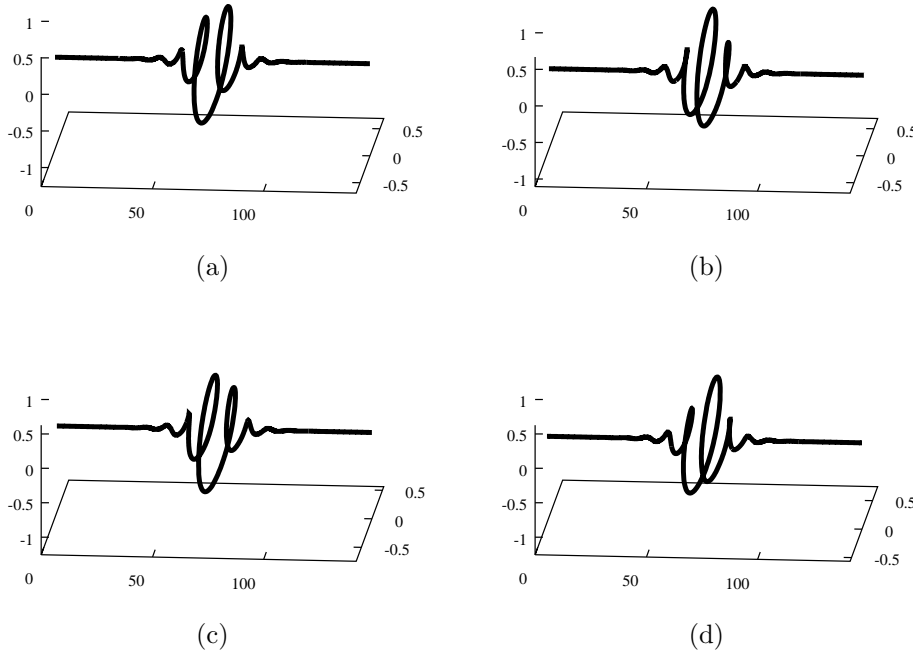


FIG. 3.1. The four primary buckling modes for $\nu = \frac{1}{3}$, $\rho = 0.5$, $m = 1.7$ shown in physical space.

from such limits, nondegeneracy conditions are hard to check analytically and so in what follows we shall investigate the structure of multimodal solutions numerically, extending the preliminary findings of [9].

We start by numerically demonstrating the existence of several infinite families of bimodal orbits, that is, homoclinic solutions which resemble two primary orbits separated by a finite number of oscillations. Specifically, for the same parameter values as above, we have found whole series of related bimodal homoclinic orbits with increasing midpoint \mathcal{T} (see Tables 3.2 and 3.3). Table 3.2 contains data pertaining to R_1 -reversible solutions with P_1 humps, that is, solutions which resemble two copies of the primary homoclinic orbit P_1 separated by a finite number of small-amplitude oscillations. In physical coordinates, such a solution looks like two large-amplitude helical deformations connected by smaller-amplitude helical oscillations (see Fig. 3.2). We shall label such solutions as (P_1, n, P_1) , where n is a measure of the number of helical oscillations between the two large helices. The choice of origin for n is somewhat arbitrary. Table 3.2 presents the δ and \mathcal{T} values for 15 such orbits with increasing n . Notice that the δ values converge to that of the primary orbit P_1 given in Table 3.1, while the difference between successive \mathcal{T} values tends to $\frac{\pi}{2\omega}$ (as was the case for a similar sequence in [7]). This can be understood by imagining each successive homoclinic orbit in the sequence making an extra quarter turn around the origin immediately prior to hitting the symmetric section (see Fig. 3.3 which shows plots of the first four solutions of Table 3.2 up to the point where they reach the symmetric section).

We could find a similar sequence of R_1 -reversible solutions whose initial hump is

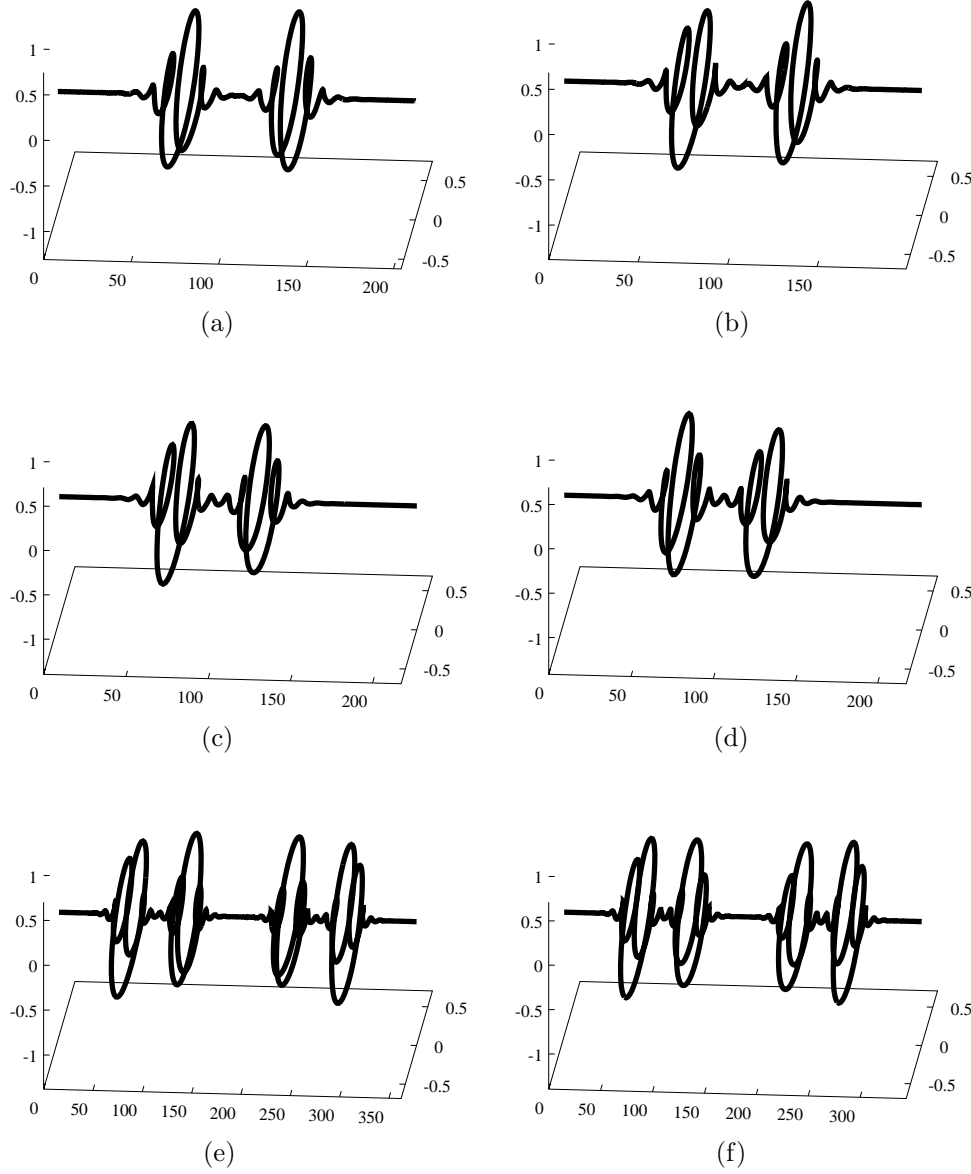


FIG. 3.2. The spatial configuration of some multimodal buckling modes for $\nu = \frac{1}{3}$, $\rho = 0.5$, $m = 1.7$: (a) the bimodal $(P_3, 3, P_4)$, (b) the bimodal $(P_1, 3, P_2)$, (c) the nonreversible bimodal $(P_1, 3, P_3)$, (d) the nonreversible bimodal $(P_2, 3, P_4)$, (e) the 4-modal $(P_1, 3, P_2, 12, P_2, 3, P_1)$, (f) the 4-modal $(P_1, 3, P_3, 12, P_4, 3, P_1)$.

of the form of the primary orbit P_3 . Table 3.3 gives some selected data. Noticing that $R_1 : P_3 \rightarrow P_4$, we label such bimodal orbits by strings of the form (P_3, n, P_4) . Table 3.3 also contains data for R_2 -reversible bimodals with first humps of the form P_1 and P_3 , labeled (P_1, n, P_2) and (P_3, n, P_3) , respectively. Note that the properties of accumulation of δ values on that of the primary orbit and the increase in \mathcal{T} values

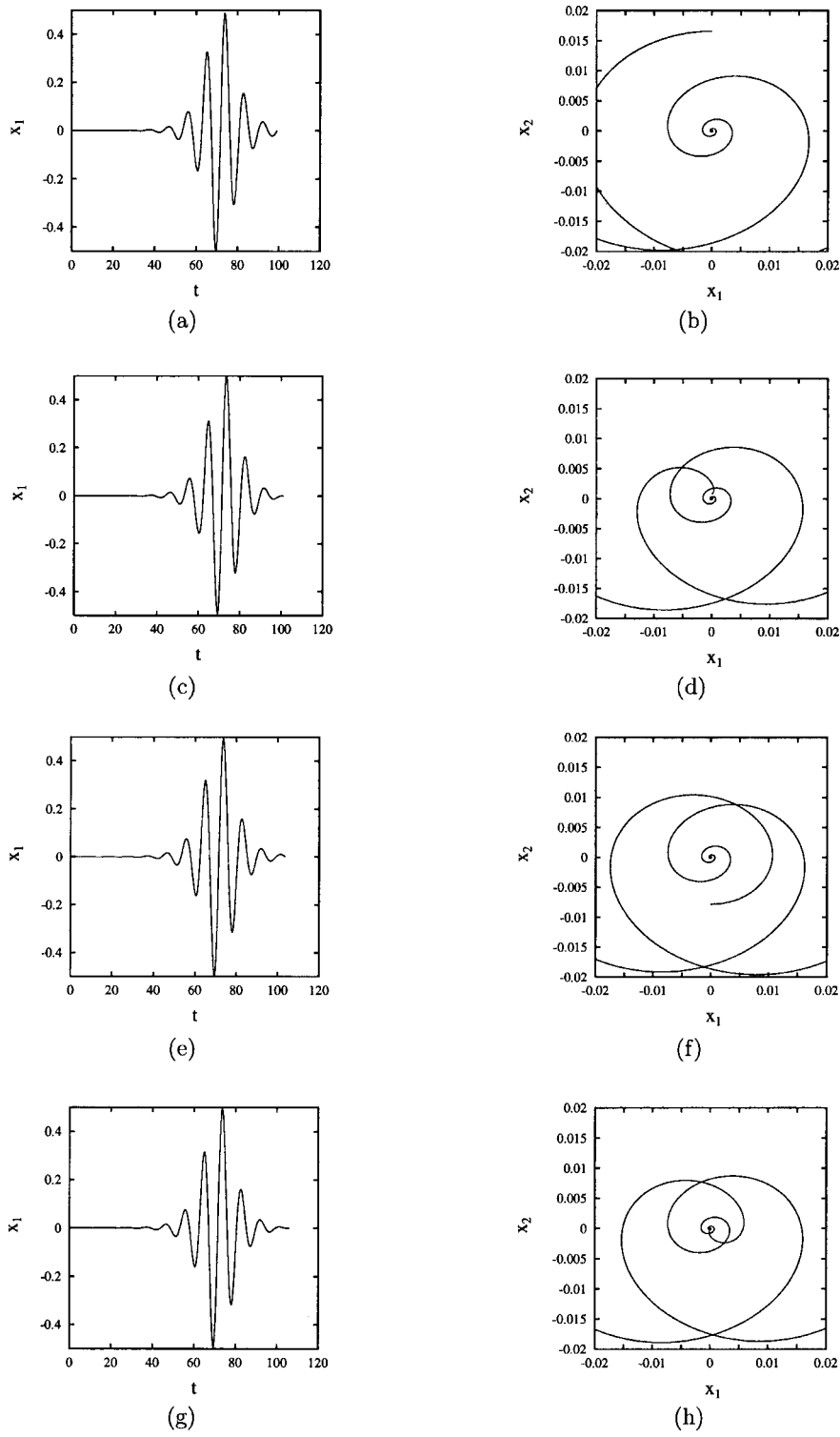


FIG. 3.3. Graphs (left) and phase space enlargements (right) of the first four bimodals (P_1, n, P_1) of Table 3.2 ($\nu = \frac{1}{3}$, $m = 1.7$, $\rho = 0.5$).

TABLE 3.3

Sequence of R_1 -reversible bimodal homoclinic orbits with labels (P_1, n, P_1) (see text for explanation of labeling) for $\nu = \frac{1}{3}$, $\rho = 0.5$, $m = 1.7$.

Sequence	n	δ_n	\mathcal{T}_n	$\mathcal{T}_n - \mathcal{T}_{n-1}$
(P_3, n, P_4) (R_1 -reversible)	1	1.498467	99.106895	
	15	1.331792	131.408103	2.324944
	P_3	1.331789	71.467436	$\frac{\pi}{2\omega} = 2.324928$
(P_1, n, P_2) (R_2 -reversible)	1	0.150328	97.105229	
	15	6.066436	129.112558	2.324963
	P_1	6.066428	71.498592	$\frac{\pi}{2\omega} = 2.324928$
$P_3, n, P_3)$ (R_2 -reversible)	1	1.682131	97.054390	
	15	1.331796	129.083181	2.324963
	P_3	1.331789	71.467436	$\frac{\pi}{2\omega} = 2.324928$
$(P_1, 3, P_2, n, P_2, 3, P_1)$ (R_1 -reversible)	1	6.150926	158.440689	
	15	6.147404	190.985739	2.324928
	$(P_1, 3, P_2)$	6.147404	101.332649	$\frac{\pi}{2\omega} = 2.324928$
$(P_1, 3, P_3, n, P_4, 3, P_1)$ (R_1 -reversible)	1	0.0343454	149.387747	
	15	0.0692012	181.990639	2.324925
	$(P_1, 3, P_3)$	0.0692018	220.121647	$\frac{\pi}{2\omega} = 2.324928$

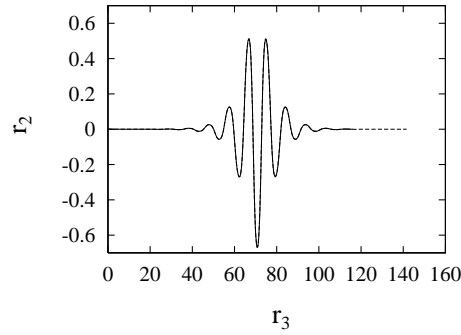


FIG. 3.4. Superposition of the primary orbit P_3 (dashed line) and half the bimodal orbit $(P_1, 10, P_2)$ (solid line), illustrating the accumulation of bimodals onto primaries in physical space ($\nu = \frac{1}{3}$, $\rho = 0.5$, $m = 1.7$).

by an approximate constant are again obeyed.

In addition to the four sequences of bimodal solutions so far presented, each of the solutions in these series has a Z partner with δ differing by π . Such sequences would have labels (P_2, n, P_2) , (P_4, n, P_3) , (P_2, n, P_1) , and (P_4, n, P_4) . Thus there appear to be eight distinct families of *reversible* bimodal buckling modes. In phase space each series of bimodal orbits accumulates on their two respective primary orbits with increasing n . In physical space (x, y, z) they converge to a perfect match with the primary orbit shapes, indicating that bimodal buckling modes may really be considered as pairs of primaries. To illustrate this, in Fig. 3.4 we have plotted, in a planar projection of physical space, the primary orbit P_1 together with the bimodal $(P_1, 10, P_2)$ up to the point where it hits the symmetric section. The match for $n = 10$ is already so good that the two can barely be distinguished.

Recall that the shooting method described above only finds reversible homoclinic orbits because we are shooting into the symmetric section of either of the involutions R_1 or R_2 . Nonreversible homoclinic orbits also exist, however, as Figs. 3.2c and d show: the bimodal $(P_1, 3, P_3)$ was obtained by shooting over the whole length of the

rod using boundary conditions which project out the unstable directions. Its Z partner (or the 180° rotated rod) can again be obtained by adding π to δ , and this solution is shown in Fig. 3.2d. In all, we have $4^2 = 16$ sequences of bimodals, 8 of which are reversible. It would seem that a small extension to Devaney's construction [12] under the assumption of four primary orbits and appropriate transversality conditions could be used to show the existence of all 8 of these sequences. For brevity, we do not pursue this analytical construction in detail here.

We would expect the method of counting multimodal orbits to extend to solutions with more and more large deflections or “humps.” Thus there should be 64 sequences of trimodal orbits consisting of a chain of three primary orbits separated by arbitrary numbers of small oscillations in phase space. Each sequence is parametrized by two integers representing the numbers of small oscillations. Only a small subset of such orbits will be reversible (namely, those for which (i) the number of oscillations before the middle hump is equal to the number after, and (ii) the humps are of the “right” type). Thus for any positive integer n we conjecture the existence of 4^n families of n -modals, each family parametrized by $n - 1$ integers, of which $2 \times 4^{n/2}$ are reversible if n is even and $4 \times 4^{[n/2]}$ are reversible if n is odd (here $[i]$ denotes the integer part of i).

Selected data for two particular families of reversible 4-modal solutions are included in Table 3.3. The first sequence has labels of the form $(P_1, 3, P_2, n, P_2, 3, P_1)$, and its solutions accumulate, as $n \rightarrow \infty$, on copies of the bimodal orbits $(P_1, 3, P_2)$ and $(P_2, 3, P_1)$. Note that the δ values converge on that for the bimodal orbit $(P_1, 3, P_2)$ as they should. The second sequence of 4-modals in Table 3.3 has labels of the form $(P_1, 3, P_3, n, P_4, 3, P_1)$, and solutions accumulate on the bimodal orbits $(P_1, 3, P_3)$ and $(P_4, 3, P_1)$. Note that these bimodals are not themselves reversible and hence do not appear in Tables 3.2 and 3.3. In fact, the bimodal $(P_1, 3, P_3)$ is the nonreversible orbit shown in Fig. 3.3c and it could be computed easily by using the second sequence of 4-modals listed in Table 3.3.

4. Continuation of homoclinic orbits.

4.1. Load-deflection diagrams. In this section we present continuation results obtained by using the software package AUTO, in particular its boundary-value problem solver. Because we are interested in load-deflection characteristics of the various solutions, we monitor the end displacement D and end rotation R , as defined in (3.7), along the computed solution branches as parameters are varied. Now, since in our shooting method we are computing homoclinic orbits up to the point where they hit the symmetric section, a problem occurs in computing the end rotation, since the local coordinate frame at the intersection point need not be aligned with the initial frame, i.e., $\mathbf{e}_3(\mathcal{T}) \neq \mathbf{e}_3(0)$. This is particularly the case for the primary orbits (and for all solutions with an odd number of humps). Therefore, in order to get meaningful end rotation results we started our continuations from a solution specified over the full length (obtained by our shooting method using projection boundary conditions).

Further, to allow a comparison of end rotations for different solutions, we eliminate the effects due to the difference in lengths \mathcal{T} by subtracting from R the end rotation R_0 the straight, unbuckled rod would have. Since for the straight rod we have $\mathbf{x} = \mathbf{0}$, the Frenet–Serret equations (2.6) give

$$\ddot{\mathbf{e}}_{1,2} = -(1 + \nu)^2 \mathbf{e}_{1,2}.$$

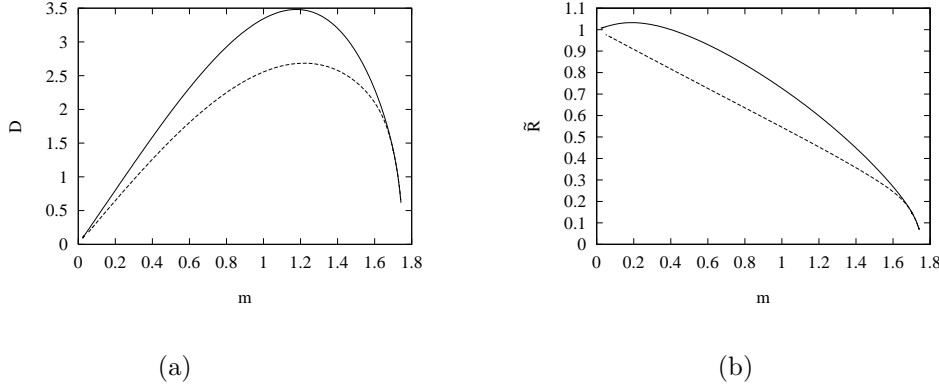


FIG. 4.1. (a) End shortening D and (b) relative end rotation \tilde{R} versus load m for the primary homoclinic orbits. Solid lines pertain to P_1 and P_2 , dashed lines to P_3 and P_4 in Table 3.1. ($\nu = \frac{1}{3}$, $\rho = 0.5$, implying $m_{c_2} = 1.751187$.)

It follows that, for a rod of length \mathcal{T} , the angle turned by the end point is given by

$$R_0 = (1 + \nu)\mathcal{T}.$$

We now define the relative end rotation \tilde{R} by

$$\tilde{R} = \frac{R - R_0}{2\pi}.$$

Thus, \tilde{R} represents the pure buckling contribution to the rod's end rotation.

Bifurcation diagrams for the primary solutions of Table 3.1 are given in Fig. 4.1, showing both D and \tilde{R} as m is varied. For $\rho = 0.5$ the two bifurcation lines depicted in Fig. 2.1 occur at $m_{c_1} = 0.155739$ and $m_{c_2} = 1.751187$. Note that only the latter value corresponds to a Hamiltonian–Hopf bifurcation. The former corresponds to a point where four complex eigenvalues become real. Notice that curves for the primary homoclinic orbits terminate in Hamiltonian–Hopf points. Figure 4.2 shows, on a scaled “time” interval $[0,1]$, how a primary solution changes shape when approaching the bifurcation point. The curves in this figure represent data for $\mathcal{T} = 150$ obtained after an initial continuation in \mathcal{T} in order to get better results close to buckling. Solutions plotted on varying m toward a Hamiltonian–Hopf bifurcation look similar (cf. [9, Fig. 2] for the case when $\rho = 0$).

Now we turn to the multimodal homoclinic orbits and try to find some structure in the multitude of multimodal buckling solutions (as was found to exist for the strut in [4]). We will do this by concentrating on one family of multimodals in particular, for which we take the bimodal orbits of Table 3.2. Continuation results for the first eight of these bimodals are given in Fig. 4.3.

We make the following observations. In both diagrams of Fig. 4.3 the curves for bimodal solutions approximately fall on top of each other: Individual bimodals differ only in the number of small oscillations made around the fixed point before reaching the symmetric section, and these have only little effect on the end shortening D and the relative end rotation \tilde{R} . *Because bimodals essentially comprise two copies of primaries, it should also not be surprising that D and \tilde{R} values for the bimodals are roughly double those for the primaries.* Bimodals taken from other sequences are found to yield essentially the same load-deflection curves.

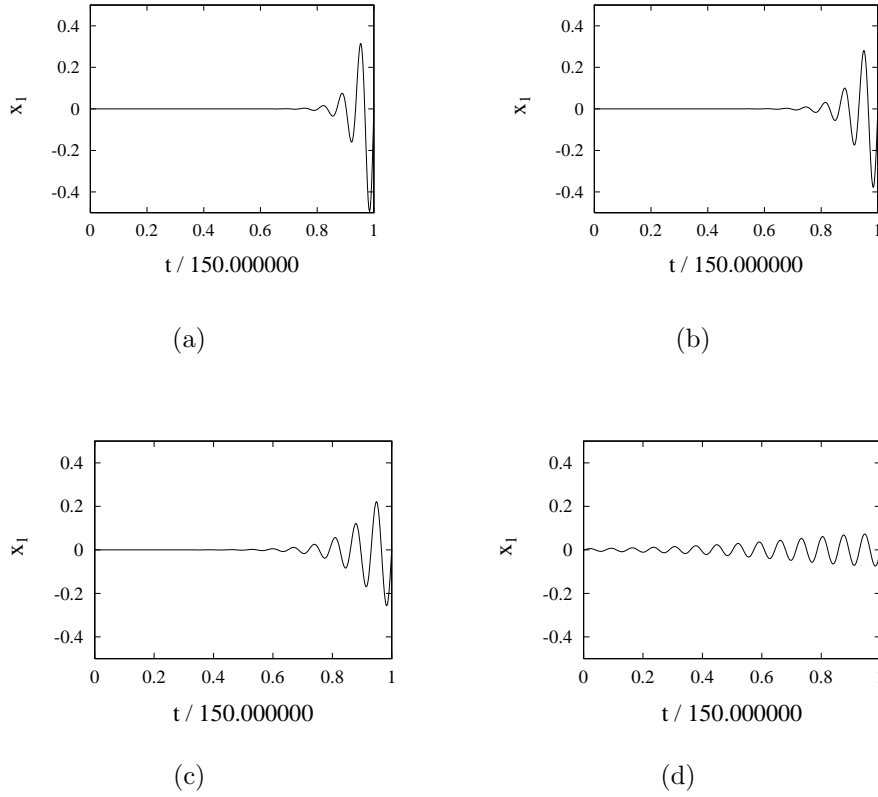


FIG. 4.2. The primary solution P_1 for various values of ρ approaching the Hamiltonian–Hopf bifurcation located at $\rho_{\text{Hopf}} = 0.601660$: (a) $\rho = 0.5$, (b) $\rho = 0.55$, (c) $\rho = 0.58$, (d) $\rho = 0.6$ ($\nu = \frac{1}{3}$, $m = 1.7$).

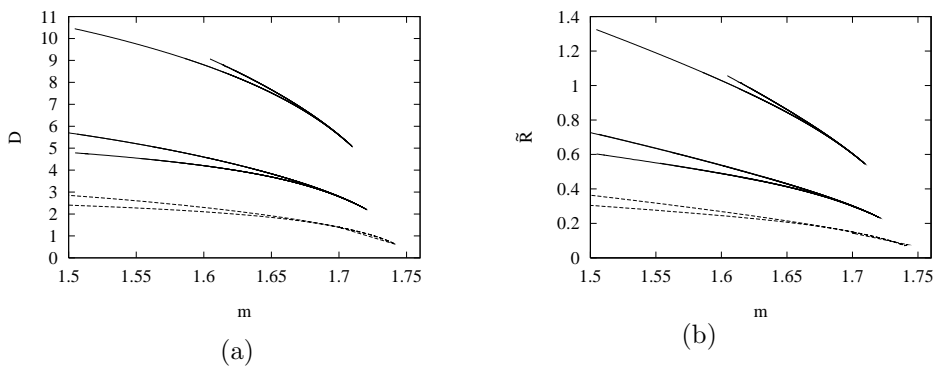


FIG. 4.3. (a) End shortening D and (b) relative end rotation \tilde{R} versus load m for the first eight bimodals (P_1, n, P_1) of Table 3.2 as well as the first six 4-modals ($P_1, 3, P_2, n, P_2, 3, P_1$). Curves for the primary orbits are included in dashed lines for comparison. Note that D and \tilde{R} values for the 4-modals are roughly double those for the bimodals which, in turn, are roughly double those for the primaries, as should be expected. ($\nu = \frac{1}{3}$, $\rho = 0.5$.)

TABLE 4.1

Limit points (LP) in the continuation of the bimodals (P_1, n, P_1) listed in Table 3.2. Continuations in ρ are for $m = 1.7$ (implying $\rho_{\text{Hopf}} = 0.601660$); those in m are for $\rho = 0.5$ (implying $m_{c_2} = 1.751187$).

n	LP (continuation in ρ)		LP (continuation in m)
1	0.000157	0.519997	1.707090
2	0.000157	0.520493	1.707273
3	0.000015	0.534112	1.712839
4	0.000015	0.534305	1.712917
5	0.000001	0.543809	1.717187
6	0.000001	0.543891	1.717222
7	0.000000	0.550928	1.720601
8	0.000000	0.550965	1.720617
9	0.000000	0.556399	1.723359
10	0.000000	0.556416	1.723367

All bimodal orbits give load-deflection curves which show a limit point to the right (at a value m just smaller than m_{c_2}) and end points to the left where the continuation breaks down due to poor convergence. Inspection of the solutions near such points suggests that these convergence problems are related to peaks becoming too large and too sharp for the continuation code to deal with (see [7], where similar problems were encountered).

We have also done continuations in the parameter ρ . The results are similar to the m curves in Fig. 4.3, with limit points just before the Hamiltonian–Hopf bifurcation. The ρ curves, however, are closed, with the leftmost limit point occurring for very small values of ρ . This makes sense because for $\rho = 0$ our system is completely integrable and we know that no multimodal homoclinic orbits then exist. Parameter values at which the limit points occur are listed in Table 4.1.

The information contained in Table 4.1 and Fig. 4.3 is further elucidated in the following subsection, which attempts to spot some patterns in what is observed.

4.2. Rules for coalescence. From the continuation results for the bimodals of Table 3.2 some pattern can be discerned. As can be seen from Table 4.1, for increasing n the closed ρ curves become wider; i.e., the left-hand limit point moves closer to $\rho = 0$ and the right-hand limit point moves closer to ρ_{Hopf} . So, in going to the integrable limit ($\rho = 0$) the higher-order orbits that make more turns around the trivial fixed point survive for longer. The limit points on the m curves also move to higher parameter values with increasing n .

Superimposed on this trend for increasing n there clearly exists a pairing of solutions: the bifurcation values for the solutions in Table 4.1 with labels $2k + 1$ and $2k + 2$, for any fixed k , are closer to each other than to those of preceding or following solutions in the series.

On all curves in Fig. 4.3, the starting solution from Table 3.2 is found to occupy the upper branch. When actually plotting different solutions on a common branch in an x_1 - t diagram (see Fig. 4.4), we observe that in the limit points solutions with different labels coalesce. Specifically, solutions with even humps coalesce with solutions with odd humps, and vice versa. Moreover, the precise pairing of solutions depends on whether n is even or odd.

Put more generally, we deduce the following rules for bimodal homoclinic orbits: *For the R_1 -reversible bimodals the following pairs of solutions share branches and co-*

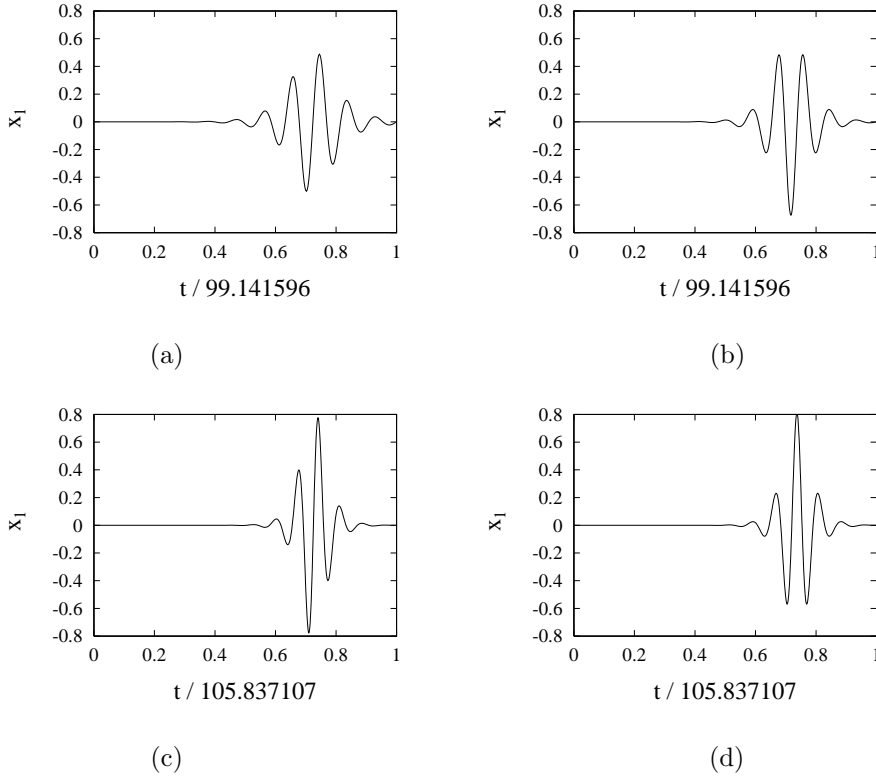


FIG. 4.4. *Coalescing R_1 -reversible bimodal homoclinic orbits: (a) orbit $(P_1, 1, P_1)$, at $\rho = 0.5$; (b) orbit $(P_3, 1, P_4)$, at $\rho = 0.4089$; (c) orbit $(P_1, 4, P_1)$, at $\rho = 0.1702$; (d) orbit $(P_4, 4, P_3)$, at $\rho = 0.2381$. (a) coalesces with (b), while (c) coalesces with (d). ($\nu = \frac{1}{3}$, $m = 1.7$.)*

alesce at limit points (for continuation in m as well as in ρ):

$$\begin{aligned}
 (P_1, 2k+1, P_1) &\longleftrightarrow (P_3, 2k+1, P_4), \\
 (P_1, 2k+2, P_1) &\longleftrightarrow (P_4, 2k+2, P_3), \\
 (P_2, 2k+1, P_2) &\longleftrightarrow (P_4, 2k+1, P_3), \\
 (P_2, 2k+2, P_2) &\longleftrightarrow (P_3, 2k+2, P_4).
 \end{aligned}$$

Similarly, for R_2 -reversible bimodals the following pairs of solutions coalesce:

$$\begin{aligned}
 (P_1, 2k+1, P_2) &\longleftrightarrow (P_3, 2k+1, P_3), \\
 (P_1, 2k+2, P_2) &\longleftrightarrow (P_4, 2k+2, P_4), \\
 (P_2, 2k+1, P_1) &\longleftrightarrow (P_4, 2k+1, P_4), \\
 (P_2, 2k+2, P_1) &\longleftrightarrow (P_3, 2k+2, P_3).
 \end{aligned}$$

Thus, for bimodal buckling modes the “coalescence rules” seem simple. The matter becomes more involved when considering buckling shapes with three or more humps so that combinations of different types of humps, with various numbers of small oscillations in between, become possible. As an example, coalescing 4-modal solutions are depicted in Fig. 4.5. Again, there is a dependence on whether n is even or odd (a trend which continues to hold for larger n). Some (parts of) bifurcation curves are included in Fig. 4.3. Continuation proves to be even more difficult for 4-modals than

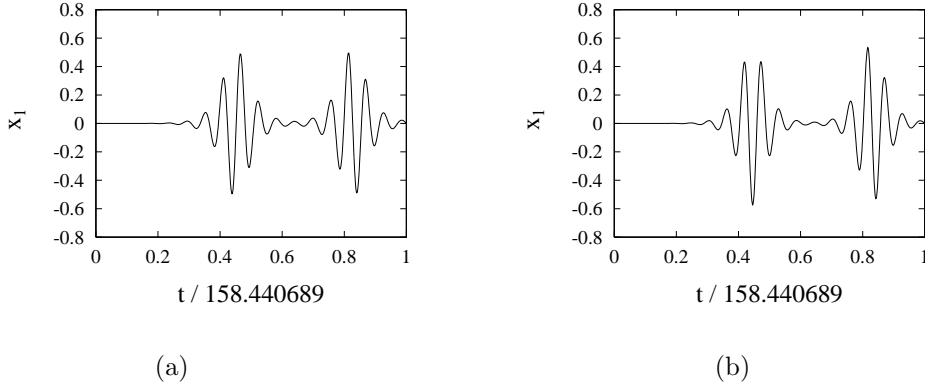


FIG. 4.5. The coalescing R_1 -reversible 4-modal homoclinic orbits (a) $(P_1, 3, P_2, 1, P_2, 3, P_1)$ at $\rho = 0.5$ and (b) $(P_3, 3, P_2, 1, P_2, 3, P_4)$ at $\rho = 0.4780$ ($\nu = \frac{1}{3}$, $m = 1.7$).

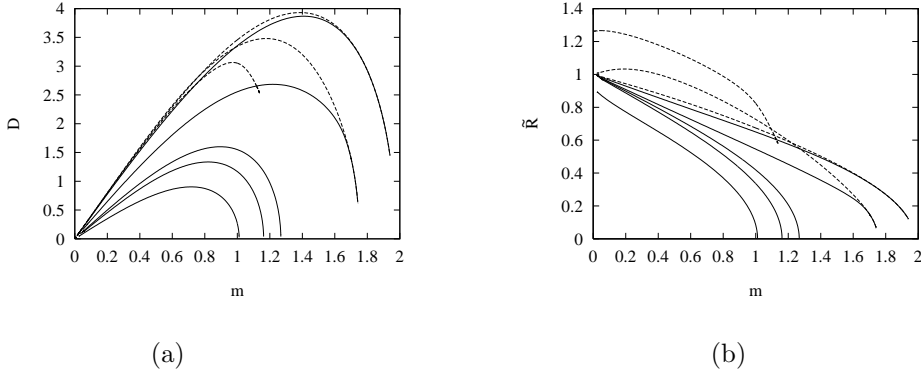


FIG. 4.6. (a) End shortening D and (b) relative end rotation \tilde{R} versus load m for the primary homoclinic orbits at several values of ρ . Solid lines pertain to the mode P_3 (and P_4); dashed lines represent (less complete) data for P_1 (and P_2). ρ values are, from right to left, 0.05, 0.5, 1.5, 2.0 and 4.0 ($\nu = \frac{1}{3}$, implying $m_{c2,3} = 1.975035, 1.751187, 1.267731, 1.161895$ and 1.011300 , respectively).

it is for bimodals. Presumably the ρ curves are still closed, but continuation breaks down before reaching the leftmost limit point. Note that D and \tilde{R} values for the 4-modals, again practically the same for all species, are roughly double those for the bimodals, as expected. Also, limit points for the 4-modals occur to the left of those for the bimodals; so, 4-modals vanish “before” bimodals, which in turn vanish “before” the primaries.

In principle one can go on to find coalescence rules for higher-order multimodals in a way quite similar to, but computationally more demanding than the case of the strut in [4]. The experience from [4] was, though, that actually proving these rules found numerically is virtually impossible. Therefore, we will not pursue this further here.

4.3. Global two-parameter investigation. Thus far we have been considering only the region in the parameter plane around $\rho = 0.5$, $m = 1.7$ (cf. Fig. 2.1). In order to investigate regions with significantly larger ρ we took the primary solution P_3 , continued it first from $m = 1.7$ to $m = 1.0$, and subsequently increased ρ beyond ρ_c and ρ_{\max} . It turns out that P_3 can be continued all the way up to the line m_{c3} , which, for $m = 1.0$, is reached for $\rho = 4.333333$. Note that crossing the line m_{c1} does

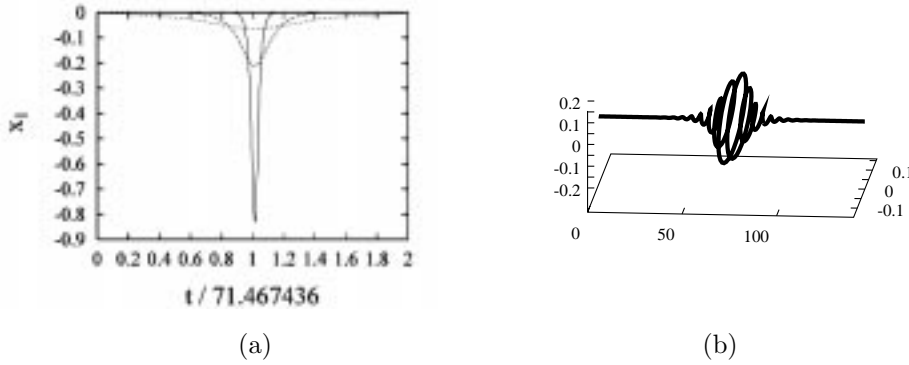


FIG. 4.7. (a) The primary solution P_3 for three values of ρ approaching the “Hamiltonian pitchfork” bifurcation located at $\rho = 4.333333$: $\rho = 2.0$ (solid curve), $\rho = 4.0$ (dashed curve), and $\rho = 4.3$ (dotted curve). (b) The corresponding physical rod shape for $\rho = 4.0$. ($\nu = \frac{1}{3}$, $m = 1.0$.)

not represent a bifurcation of the zero solution; it just means that the eigenvalues become real.

Figure 4.6 shows load-deflection diagrams for different values of ρ . Besides data for three larger ρ values we have included our previous results for $\rho = 0.5$ as well as results for a smaller value, $\rho = 0.05$, which, in section 5, will be used to discuss the integrable limit of a symmetric rod ($\rho = 0$). For increasing m all curves with $\rho > \rho_c$ terminate at m_{c3} , where we have a “Hamiltonian pitchfork” bifurcation and both D and \tilde{R} drop to zero. (Note that some of the presented curves do not reach zero owing to the large value of the truncation interval \mathcal{T} required.) The same type of bifurcation is encountered for increasing ρ . Several instances of this latter approach to m_{c3} , in the form of x_1 - t diagrams, are depicted in Fig. 4.7a. The figure clearly shows the monotonic decay of solutions close to the bifurcation, consistent with the fact that all eigenvalues of the trivial fixed point are real. Figure 4.7b shows the corresponding physical rod shape for one particular value of ρ . It is seen that the spatial configuration of the rod is still helical, a property which is now solely the result of feeding the solution in Fig. 4.7a through the Frenet–Serret equations (2.6). The monotonic decay in Fig. 4.7a may be compared with the oscillatory behavior of solutions in the approach to a Hamiltonian–Hopf bifurcation, as exemplified by Fig. 4.2. It would be instructive in further work to examine the physical and experimental aspects of this change in behavior as ρ passes ρ_c . Some results are reported in [25].

Some continuation data for the primary solution P_1 is included in dashed lines in Fig. 4.6. As long as $\rho < \rho_c$ (here, $\rho_c = 1.1064$), the load-deflection diagrams for both modes terminate at the same buckling value for m . However, as explained in [25], for $\rho > \rho_c$, the P_1 mode does not bifurcate from the trivial solution and, consequently, the curves in Fig. 4.6 do not drop to zero. A notable difference between the two buckling modes is that P_1 gives rise to larger D and \tilde{R} values and that this effect rather sharply increases with increasing ρ . We further observe that for both modes the end shortening and relative end rotation decrease with increasing ρ . In the limit $\rho = 0$ the curves for P_1 and P_3 become identical.

We were unsuccessful in attempts to continue a multimodal orbit beyond ρ_{\max} . As argued in section 5, this is consistent with the loss of multiplicity in homoclinic solutions expected upon crossing m_{c1} , when the eigenvalues of the origin become real. Recall, however, that continuation in m led to convergence problems earlier.

5. Discussion and physical interpretation. Our extensive numerical investigations have revealed a vast complexity of localized buckling modes in twisted rods, as was already conjectured to be the case in [9] on the basis of an analogy with the problem of a strut resting on a nonlinear elastic foundation. In principle it is possible to uncover structure in the multitude of multimodal buckling solutions, as we showed explicitly for the bimodals and briefly touched on for the 4-modals.

Breaking the circular symmetry of the rod causes a splitting of the primary localized buckling mode into two modes which have different load-deflection characteristics. Moreover, this difference increases sharply with increasing values of the anisotropy parameter ρ . Mathematically, buckling in twisted rods occurs in two different ways. For $\rho < \rho_c$ buckling is described by a Hamiltonian–Hopf bifurcation. Normal-form theory explains the emergence of four homoclinic orbits, here denoted P_1 , P_2 , P_3 , and P_4 , from this bifurcation. In contrast, for $\rho > \rho_c$ (“tapes”) buckling occurs through a Hamiltonian pitchfork bifurcation. So the “buckling line” in the parameter plane of Fig. 2.1 is formed by the union of m_{c_2} and the large- ρ part of m_{c_3} . The two types of buckling greatly differ in the complexity of the underlying homoclinic structure: The tape is less complex than the mildly anisotropic.

In trying to piece together the global bifurcation diagram of localized buckling modes in the two-parameter plane of Fig. 2.1, we note the similarities with yet another problem, namely, the problem of steady water waves in the presence of surface tension [18, 19]. There, in the parameter space of Bond versus Froude number the two-parameter bifurcation diagram of the trivial equilibrium is qualitatively equivalent to Fig. 2.1, including a point analogous to the codimension-2 point at $\rho = \rho_c$. Recently, in [10] a two-degrees-of-freedom reversible Hamiltonian system was considered that contains the same linearization as the full water-wave problem. By analogy with the global two-parameter analysis of homoclinic solutions of that system we can make the following general statements about what we generically expect to occur for the twisted rod equations.

An abundance of multimodal buckling shapes exist for parameters for which the eigenvalues of the trivial equilibrium form a complex quadruple, consistent with Devaney’s theory. Because the normal-form analysis of the Hamiltonian–Hopf bifurcation does not allow multimodal solutions, all multimodals must disappear when approaching the line m_{c_2} in Fig. 2.1. This is realized by the limit points in Fig. 4.3. Similarly, multimodals are known not to exist for the symmetric rod ($\rho = 0$), which necessitates the leftmost limit points along ρ curves listed in Table 4.1, although the ρ values at which they occur are extremely small. Coalescence rules specifying which solutions annihilate in these limit points somehow reflect the relative location of solutions in the stable and unstable manifolds of the trivial equilibrium. A better knowledge of this structure of solutions in the invariant manifolds would presumably allow us to make inferences about the bifurcation sequences that can occur, in particular the order in which homoclinic solutions have to vanish in limit points.

When the eigenvalues of the origin are real (in the region of Fig. 2.1 to the right of m_{c_1} and below m_{c_3}), one should not expect to see multiplicities of multimodal solutions. There are, however, certain mechanisms that may give rise to finitely many multimodal solutions with a given number of humps; see [10] for references. Thus, for sufficiently large ρ , upon decreasing m through the Hamiltonian pitchfork line m_{c_3} we would expect to see only the primary buckling modes and possibly finitely many multimodal ones of each modality.

It follows from the above that upon crossing the line m_{c_1} we should expect to

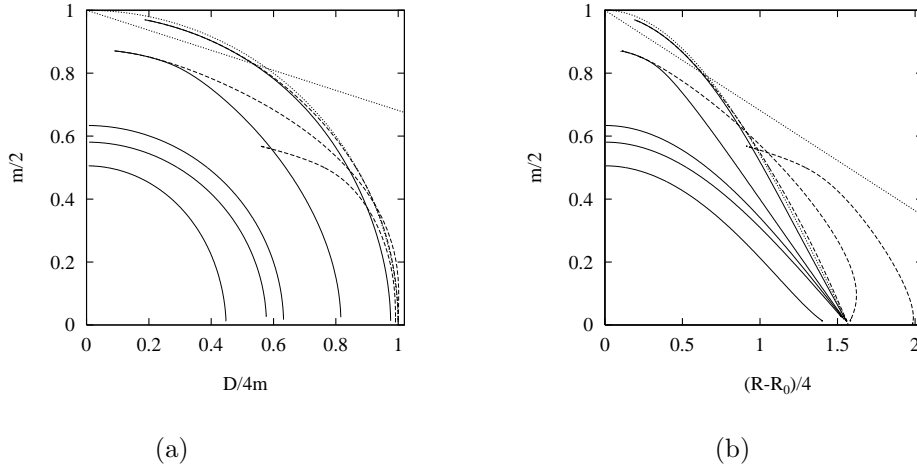


FIG. 5.1. Load-deflection diagrams for the primary buckling modes P_3 (and P_4) (solid lines) and P_1 (and P_2) (dashed lines) for (from right to left) $\rho = 0.05, 0.5, 1.5, 2.0$, and 4.0 , compared with those for Coyne's localized mode (dotted curved lines) and the helix (dotted straight lines), the latter two both for the symmetric rod, i.e., $\rho = 0$ ($\nu = \frac{1}{3}$).

see the sudden disappearance of infinite classes of multimodal homoclinic orbits. One should expect this to occur through the “Devaney–Belyakov” mechanism described for a certain class of Hamiltonian systems in [8]. One characteristic of such an event is that the humps of the multimodal solutions move apart with speed tending to infinity as the bifurcation is approached. It is this rapid separation that is behind the earlier remarked loss of convergence in the numerical continuation with decreasing m .

In [24] the authors compared load-deflection diagrams for the helical and Coyne's localized buckling modes in symmetric rods. To facilitate a comparison of these results with ours obtained for nonsymmetric rods we have plotted in Fig. 5.1 our results for the primary orbits presented in Fig. 4.6 together with the results of [24], adopting the plot variables used in [24]. For the localized mode in symmetric rods the end displacement and end rotation are given by

$$\frac{D^2}{16m^2} + \frac{m^2}{4} = 1, \quad \cos \frac{R - R_0}{4} = \frac{m}{2},$$

while the corresponding quantities for a helix (evaluated over one helical turn) are

$$\frac{D}{4m} = \pi \left(1 - \frac{m}{2}\right), \quad \frac{R - R_0}{4} = \pi \left(1 - \frac{m}{2}\right),$$

yielding the straight lines in Fig. 5.1.

The data for a rod with very small anisotropy ($\rho = 0.05$) included in Fig. 5.1 shows that in the limit of small ρ the analytically known behavior of a symmetric rod is nicely recovered, all primary modes acquiring the same load-deflection characteristics.

Figure 5.2 attempts to give a physical explanation of our results. It turns out that the different behavior of P_1 and P_3 observed in Figs. 4.6 and 5.1 can be related to different orientations of the nonsymmetric rod. A computation of the local coordinate frame shows that for the two solutions the cross sections move very nearly 90° out of

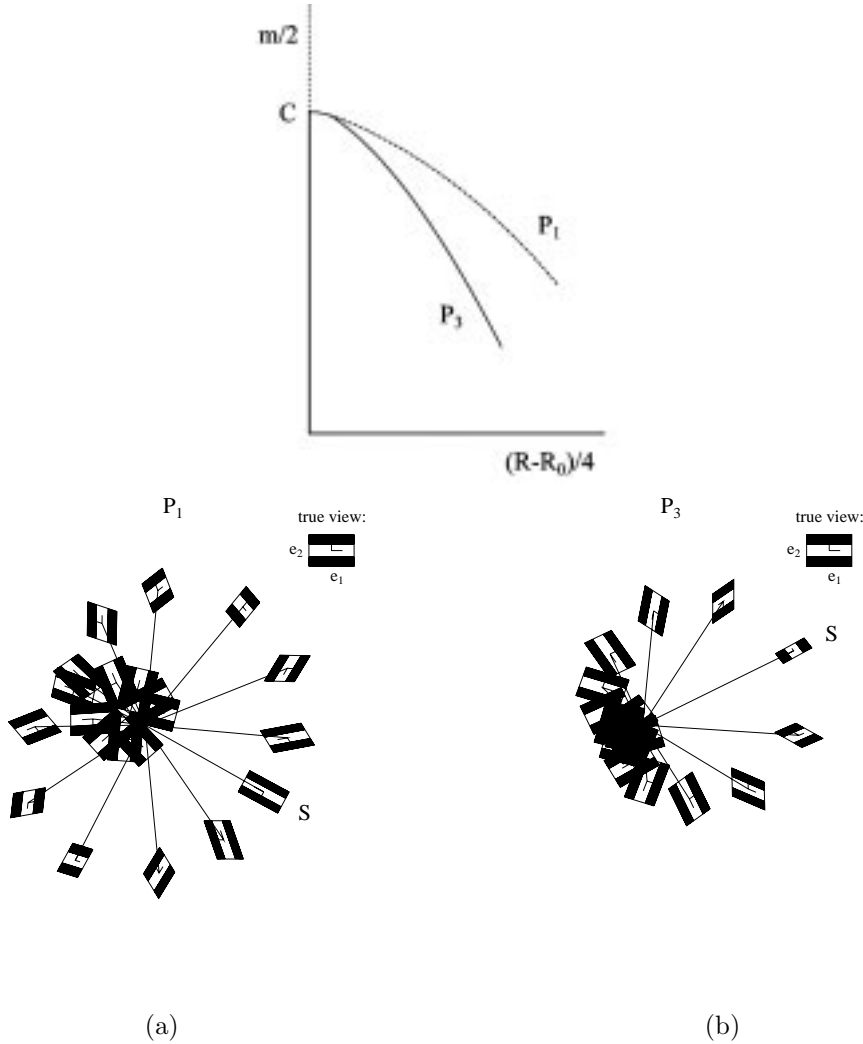


FIG. 5.2. For a rod with anisotropy parameter $\rho = 0.9$ two distinct subcritical postbuckling equilibrium paths bifurcate from the straight trivial state at the buckling load $m_{c2} = 1.5449$. One corresponds to the localized primary mode P_1 (and its Z partner P_2) and the other to the localized primary mode P_3 (and its Z partner P_4). Evolution of the orientation of the cross section in the region of large radial deflection is displayed at steps of $\Delta t \simeq 0.004$ for $m = 1.3$ (the sections labeled S are at the symmetric section). Of the two modes, the configuration of P_3 is seen to be closer to that of a "tape wound on a cylinder." We would therefore expect it to be energetically more favorable, offering a lower energy barrier against premature buckling. This is consistent with the fact that the P_3 postbuckling path falls more steeply from the bifurcation point C than the P_1 path.

phase along the centerline of the rod. In fact, including P_2 and P_4 in the discussion, successive pairs of primary buckling modes in the sequence $P_1 - P_3 - P_2 - P_4$ evolve 90° out of phase. In particular, in the symmetric section where, approximately, the rod attains its maximum deviation from the unstrained position, we have the cross sections labeled S in Fig. 5.2. For P_1 (resp., P_2) the vector e_1 (which, because $x_1 = 0$, is orthogonal to the z axis, i.e., the direction of the applied force) is approximately aligned with the projection of $-\mathbf{r}$ (resp., \mathbf{r}) on the x - y plane. Similarly, for P_3 (resp.,

P_4) the vector \mathbf{e}_2 is orthogonal to the z axis (because now $x_2 = 0$) and approximately directed along the x - y projection of $-\mathbf{r}$ (resp., \mathbf{r}).

Continuation results reveal that the relative orientation of \mathbf{r} , \mathbf{e}_1 , and \mathbf{e}_2 in the symmetric section is independent of the parameters m and ρ , so the situation in Fig. 5.2 is typical. For P_3 the cross section at the symmetric section comes out rather small because of the oblique view we are offered at the present value of $m = 1.3$. (The cross section would actually face into the paper for a short period if m were to drop below 1.1653; for comparison, in the symmetric rod this event can be exactly calculated to occur at $m = \sqrt{2} \simeq 1.4142$.) In interpreting Fig. 5.2 note further that the cross section of the rod is elongated in the \mathbf{e}_1 direction because $\rho > 0$, or $B > A$, i.e., the bending stiffness is larger about \mathbf{e}_2 than it is about \mathbf{e}_1 .

Close to buckling the center of the rod is approximately evolving along a helical path (cross sections in Fig. 5.2 roughly appear along a circle) and because of the varying relative phase along the rod, the phase at the symmetric section does not matter much. For decreasing m , however, the deformation of the rod becomes increasingly concentrated around its midpoint and the orientation of the cross section at the symmetric section becomes more important (cross sections in Fig. 5.2 appear along a spiral). In Fig. 5.2 we observe that for P_3 by the time the cross section has rotated 90° the radial deflection has decreased substantially, whereas for P_1 this is not the case. Thus we can appreciate the different load-deflection characteristics of the modes P_1 and P_2 on the one hand, and the modes P_3 and P_4 on the other.

To assess the practical importance of the multitude of multimodal buckling solutions in our model, it is essential to know their stability properties. Unfortunately, our methods do not give information on this. It seems likely that most, if not all, multimodals are unstable, but, depending on the boundary conditions applied and the loading sequence taken, perhaps some of them can be stabilized.

Carefully conducted experiments on nonsymmetric rods, similar to those on symmetric rods carried out in [24], might shed some light on the stability question and establish the physical changes of buckling behavior at ρ_c . It would also be interesting to experimentally verify the load-deflection diagrams computed in this paper, in particular with regard to the different behavior of the modes P_1 and P_3 . Further research might also include a study of the effects of shear, initial curvature, and gravity on load-deflection characteristics. We intend to take up these issues in future publications. See also [11, 25].

REFERENCES

- [1] S. S. ANTMAN, *Nonlinear Problems of Elasticity*, Springer-Verlag, Berlin, 1995.
- [2] L. A. BELYAKOV AND L. P. ŠIL'NIKOV, *Homoclinic curves and complex solitary waves*, *Selecta Math. Soviet.*, 9 (1991), pp. 219–228.
- [3] W.-J. BEYN, *The numerical computation of connecting orbits in dynamical systems*, *IMA J. Numer. Anal.*, 9 (1990), pp. 379–405.
- [4] B. BUFFONI, A. R. CHAMPNEYS, AND J. F. TOLAND, *Bifurcation and coalescence of a plethora of homoclinic orbits in a fourth-order Hamiltonian system*, *J. Dynam. Differential Equations*, 8 (1996), pp. 221–281.
- [5] A. R. CHAMPNEYS, *Subsidiary homoclinic orbits to a saddle-focus for reversible systems*, *Internat. J. Bifur. Chaos*, 4 (1994), pp. 1447–1482.
- [6] A. R. CHAMPNEYS, YU. A. KUZNETSOV, AND B. SANDSTEDE, *A numerical toolbox for homoclinic bifurcation analysis*, *Internat. J. Bifur. Chaos*, 6 (1996), pp. 867–887.
- [7] A. R. CHAMPNEYS AND A. SPENCE, *Hunting for homoclinic orbits: A shooting technique*, *Adv. Comput. Math.*, 1 (1993), pp. 81–108.

- [8] A. R. CHAMPNEYS AND J. F. TOLAND, *Bifurcation of a plethora of multimodal homoclinic orbits for autonomous Hamiltonian systems*, Nonlinearity, 6 (1993), pp. 665–721.
- [9] A. R. CHAMPNEYS AND J. M. T. THOMPSON, *A multiplicity of localized buckling modes for twisted rod equations*, Proc. Roy. Soc. London. Ser. A, 452 (1996), pp. 2467–2491.
- [10] A. R. CHAMPNEYS AND M. D. GROVES, *A global investigation of solitary-wave solutions to a two-parameter model for water waves*, J. Fluid Mech., 342 (1997), pp. 199–229.
- [11] A. R. CHAMPNEYS, G. H. M. VAN DER HEIJDEN, AND J. M. T. THOMPSON, *Spatially complex localization after one-twist-per-wave equilibria in twisted circular rods with initial curvature*, Phil. Trans. Roy. Soc. London Ser. A, 355 (1997), pp. 2151–2174.
- [12] R. L. DEVANEY, *Homoclinic orbits in Hamiltonian systems*, J. Differential Equations, 21 (1976), pp. 431–438.
- [13] E. J. DOEDEL AND J. P. KERNÉVEZ, *AUTO: Software for Continuation and Bifurcation Problems in Ordinary Differential Equations*, Applied Mathematics Report, California Institute of Technology, Pasadena, CA, 1986.
- [14] E. J. DOEDEL, H. B. KELLER, AND J. P. KERNÉVEZ, *Numerical analysis and control of bifurcation problems: (II) Bifurcation in infinite dimensions*, Internat. J. Bifur. Chaos, 1 (1991), pp. 745–772.
- [15] J. HÄRTERICH, *Cascades of reversible homoclinic orbits to a saddle-focus equilibrium*, Phys. D, 112 (1998), pp. 187–200.
- [16] G. W. HUNT, H. M. BOLT, AND J. M. T. THOMPSON, *Structural localization phenomena and the dynamical phase-space analogy*, Proc. Roy. Soc. London Ser. A, 425 (1989), pp. 245–267.
- [17] G. W. HUNT AND M. K. WADEE, *Comparative Lagrangian formulations for localized buckling*, Proc. Roy. Soc. London Ser. A, 434 (1991), pp. 485–502.
- [18] G. IOOSS, *A codimension 2 bifurcation for reversible vector fields*, Fields Inst. Comm., 4 (1995), pp. 201–217.
- [19] G. IOOSS AND K. KIRCHGÄSSNER, *Water waves for small surface tension: An approach via normal form*, Proc. Roy. Soc. Edinburgh Sec. A, 122 (1992), pp. 267–299.
- [20] G. IOOSS AND M. C. PÉROUÈME, *Perturbed homoclinic solutions in reversible 1:1 resonance vector fields*, J. Differential Equations, 102 (1993), pp. 62–88.
- [21] YU. A. KUZNETSOV, *Computation of invariant manifold bifurcations*, in Continuation and Bifurcations: Numerical Techniques and Applications, D., Roose, B. De Dier, and A. Spence eds., Kluwer, Dordrecht, the Netherlands, 1990.
- [22] A. E. H. LOVE, *A Treatise on the Mathematical Theory of Elasticity*, 4th ed., Cambridge University Press, Cambridge, 1927.
- [23] A. MIELKE AND P. HOLMES, *Spatially complex equilibria of buckled rods*, Arch. Rational Mech. Anal., 101 (1988), pp. 319–348.
- [24] J. M. T. THOMPSON AND A. R. CHAMPNEYS, *From helix to localized writhing in the torsional post-buckling of elastic rods*, Proc. Roy. Soc. London Ser. A, 452 (1996), pp. 117–138.
- [25] G. H. M. VAN DER HEIJDEN AND J. M. T. THOMPSON, *Lock-on to tape-like behaviour in the torsional buckling of anisotropic rods*, Phys. D, 112 (1998), pp. 201–224.